ADVANCED ENERGY MATERIALS
www.advenergymat.de

Addressing the Sluggish Kinetics of Sulfur Redox for High-Energy Mg–S Batteries

Zhenyou Li, Alexander Welle, Smobin Vincent, Liping Wang, Stefan Fuchs, Sibylle Riedel, Ananyo Roy, Dasari Bosubabu, Juan Maria García-Lastra, Maximilian Fichtner, and Zhirong Zhao-Karger**

A key challenge for practical magnesium–sulfur (Mg–S) batteries is to overcome the sluggish conversion kinetics of sulfur cathodes, achieving a high energy density and long-lasting battery life. To address this issue, a doping strategy is demonstrated in a model Ketjenblack sulfur (KBS) cathode by introducing selenium with a high electronic conductivity. This leads to a significantly enhanced charge transfer in the resultant $KBS_{1-x}Se_x$ cathodes, giving rise to a higher S utilization and less polysulfide dissolution. Compared to the bare S cathode, the S-Se composite cathodes exhibit a higher capacity, smaller overpotentials, and improved efficiency, serving as better benchmark compounds for high-performance Mg–S batteries. First principles calculations reveal a charge transport mechanism via electron polaron diffusion in the redox end-products, that enhances the reaction kinetics. By suppressing polysulfide dissolution in the electrolyte, the use of the $KBS_{1-x}Se_x$ cathodes also enables a more uniform anode reaction, and thereby significantly extends the cyclability of the cells. To improve the performance, further efforts are made by implementing a Mo_6S_8 modified separator into the cell. With an optimized cathode composition of $KBS_{0.86}Se_{0.14}$, the cell applying modified separator shows an improvement of capacity retention by >50% after 200 cycles.

1. Introduction

Magnesium–sulfur (Mg–S) batteries that couple an elemental S cathode with a Mg metal anode have attracted increasing research interest, due to their high theoretical energy density (3221 Wh L^{-1} and 1684 Wh kg^{-1}) as well as wide availability of the electrode materials.[1] A critical issue related to the S redox reaction in Mg–S batteries is its sluggish conversion kinetics due to the low electronic conductivity of S and MgS.[2] The kinetic hindrance leads to large voltage hysteresis upon charge and discharge, but also a low S utilization and therefore smaller capacity compared to the theoretical value.[3] Mixing S with conductive carbon can effectively promote charge transfer in the electrode.[4] However, as carbon does not conduct Mg^{2+},[5] ionic transport within the electrode is meanwhile negatively affected. To ensure sufficient Mg^{2+} mobility, the ionic pathway should be

Z. Li, S. Fuchs, S. Riedel, A. Roy, D. Bosubabu, M. Fichtner, Z. Zhao-Karger
Helmholtz Institute Ulm (HIU) Electrochemical Energy Storage
Helmholtzstraße 11, D-89081 Ulm, Germany
E-mail: zhenyou.li@kit.edu; zhirong.zhao-karger@kit.edu

Z. Li
Qingdao Institute of Bioenergy and Bioprocess Technology
Chinese Academy of Sciences
No. 189 Songling Road, Laoshan District, Qingdao, Shandong 266101, China

Z. Li
Shandong Energy Institute
Qingdao 266101, China

Z. Li
Qingdao New Energy Shandong Laboratory
Qingdao 266101, China

A. Welle
Institute of Functional Interfaces (IFG)
Karlsruhe Institute of Technology (KIT)
P.O. Box 3640, D-76021 Karlsruhe, Germany

A. Welle
Karlsruhe Nano Micro Facility (KNMFi)
Karlsruhe Institute of Technology (KIT)
P.O. Box 3640, D-76021 Karlsruhe, Germany

S. Vincent, J. M. García-Lastra
Department of Energy Conversion and Storage
Technical University of Denmark
Kongens Lyngby 2800, Denmark

L. Wang
Institute for Organic Chemistry II and Advanced Materials
Ulm University
Albert-Einstein-Allee 11, D-89081 Ulm, Germany

D. Bosubabu, M. Fichtner, Z. Zhao-Karger
Institute of Nanotechnology (INT)
Karlsruhe Institute of Technology (KIT)
P.O. Box 3640, D-76021 Karlsruhe, Germany

The ORCID identification number(s) for the author(s) of this article can be found under https://doi.org/10.1002/aenm.202302905

DOI: 10.1002/aenm.202302905

shortened. This was normally achieved by reducing the S to carbon ratio or S loading in the electrode, which leads to low practicality; whereas increasing these parameters would significantly reduce the performance of the Mg–S batteries.[2b,6]

Targeting at practical Mg–S batteries, kinetic improvement strategies that enhance the conversion and reversibility of S redox with no need of large amount of carbon are desired. Efforts made in this direction include introducing additives to the S cathode, such as copper (Cu), either in the form of nanoparticles[7] or as the current collector, [8] which could change the conversion pathway of S by forming kinetically more favorable copper (I) sulfide (Cu_2S).[9] However, a detailed investigation revealed that the beneficial effect of Cu was only achieved under the condition of a low S and Cu loading.[7] Another effective strategy was proposed to employ solvents with a high donor number in electrolytes, which could promote the solubility of the Mg sulfide species, enabling fast conversion reactions in solution.[10] However, the compatibility issue of such solvents with Mg anode and the high concentration of polysulfide in the electrolyte make it challenging to transfer this concept to a conventional full-cell setup.

In the light of the advancement of lithium-sulfur batteries,[11] selenium (Se) could be considered as a promising cathode additive to Mg–S systems. As a chalcogen element, Se is electrochemically active, and having an electronic conductivity which is >20 orders of magnitude higher than S (1×10^{-3} S m^{-1} for Se vs 5×10^{-28} S m^{-1}).[12] Notably, Se is miscible with S to form a large variety of heterocyclic S-Se compounds.[13] Therefore, the Se doping enables molecular engineering of the S_8 ring, which facilitates S redox by improving its bulk conductivity.[14] While this strategy was successfully demonstrated in Li–S batteries, it remains to be explored in Mg–S systems.[15]

In this work, we investigated the impact of Se doping on the conversion of S in Mg–S batteries, by preparing a series of S-Se compounds and studying their redox behavior in the presence of Mg^{2+}. Electrochemical tests of model Ketjenblack/S-Se composite ($KBS_{1-x}Se_x$) cathodes demonstrated an enhanced redox kinetics as evidenced by a higher achievable capacity, more prominent discharge plateaus, smaller overpotential and less severe overcharging. Among them, the $KBS_{0.86}Se_{0.14}$ cathode showed superior performance, in which the charge storage mechanism and the correlated influence on the Mg anode were thereby further investigated. As revealed by multimodal characterizations, the fast electrochemical kinetics in case of the $KBS_{0.86}Se_{0.14}$ cathode results in a higher utilization of S, leading to less polysulfide dissolution in the electrolyte, which is beneficial for Mg plating/stripping at anode. Due to more uniform Mg deposition, Mg–S cells with the $KBS_{0.86}Se_{0.14}$ cathode exhibited longer cyclability, while the reference cell with the KBS cathode suffered from the early cell failure. First principles calculations were further carried out to understand the mechanism of the improved performance with the addition of Se, revealing an enhanced charge transport via electron polaron diffusion in the redox end-products. Nevertheless, the $KBS_{0.86}Se_{0.14}$ cathode still suffered from fast capacity fading, due to polysulfide shuttling. Attempting to overcome this issue, a modified separator was additionally implemented in the cell, which increased the capacity retention by >50%.

2. Results and Discussion

2.1. Characterization of the S–Se Compounds

A series of S-Se compounds with different Se content were prepared and loaded onto a conductive carbon matrix (Ketjenblack, KB) through a one-step melt-diffusion method. According to energy-dispersive X-ray (EDX) spectra in Figure S1a–c (Supporting Information), the molar ratio of S/Se in the compounds was 0.92:0.08, 0.86:0.14, 0.62:0.38, respectively. As a result, the composites were named $KBS_{0.92}Se_{0.08}$, $KBS_{0.86}Se_{0.14}$ and $KBS_{0.62}Se_{0.38}$ thereafter, while the Se-free composite was named KBS. EDX mapping of the $KBS_{0.86}Se_{0.14}$ (Figure S1d–f, Supporting Information) showed evenly distribution of both S and Se on the carbon matrix. Similar results were obtained for the other compounds as well. Furthermore, the structure of the $KBS_{1-x}Se_x$ composites was characterized by X-ray diffraction (XRD). As shown in Figure S2 (Supporting Information), XRD patterns of all four composites (including KBS) presented only one broad peak at ≈10°, which could be assigned to the (002) reflection of graphitic carbon. No other diffraction peaks were detected, indicating amorphous nature of the S-Se compounds on the KB. In order to clarify the existence of S-Se interaction, X-ray photoelectron spectroscopy (XPS) was performed. **Figure 1**a presents high-resolution spectra of the S 2p and Se 3p region. A clear trend was observed from the spectrum of KBS to $KBS_{0.62}Se_{0.38}$ with a more prominent Se 3p signals, confirming an increase of the Se content. Deconvoluting the spectra resulted in several doublets at 163.9, 163.6, 162.2, and 161.9 eV, which correspond to S-S, S-Se, Se-S, and Se-Se interactions, respectively. Their relative atomic percentage presented in Figure S3 (Supporting Information) revealed an enhanced S-Se and Se-S interactions with higher Se content, which was further evidenced in the Se 3d spectra (Figure 1b) by the increase of a doublet at 56.0 eV.[16] In addition, the content of the redox active species (S and Se) in all the composites are in the range of 55–60 wt.%, as determined by the thermogravimetric analysis in Figure S4 (Supporting Information).

2.2. Electrochemical Advantages of the Se–S Compounds over Bare S Cathodes

To verify their kinetic advantages, the Se-S compounds were first evaluated by galvanostatic cycling in a three-electrode cell with Mg as both the counter electrode (CE) and reference electrode (RE). Magnesium tetrakis(hexafluoroisopropyloxy)borate, $Mg[B(hfip)_4]_2$,[17] was dissolved in diglyme (G2), serving as electrolyte. To alleviate the shuttle effect of polysulfide, the charging process was limited to 8 h for the bare S cathode and 10 h for the Se-doped S cathodes.

As shown in **Figure 2**a, a two-plateau feature during discharge process was evident for the KBS and the $KBS_{1-x}Se_x$ (x = 0–0.38) cathodes, which is similar to S conversion with ether-based electrolyte in Li–S batteries.[18] The plateau at higher voltage could be attributed to the reduction of $S_{8-2y}Se_{2y}$ to $MgS_{4-y}Se_y$ ($y = 4x$) with a solid-liquid phase transition. This process delivered a comparable capacity of 200–250 mAh g^{-1} for all the cathodes, indicating a kinetically favourable step. Major difference was observed at the lower voltage plateau, which represents further conversion to

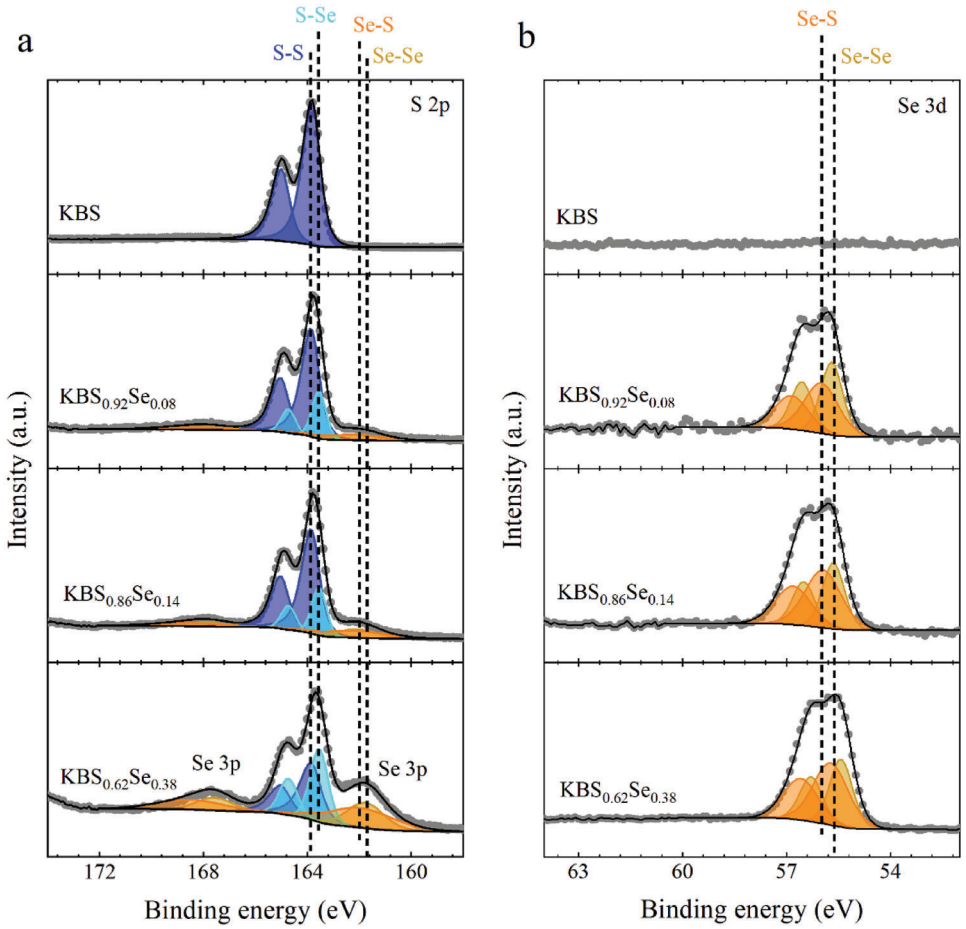

Figure 1. XPS of the KBS, $KBS_{0.92}Se_{0.08}$, $KBS_{0.86}Se_{0.14}$ and $KBS_{0.62}Se_{0.38}$ composites: a) S 2p spectra, and b) Se 3d spectra.

short-chain polysulfide/-selenides underwent a liquid-solid transition. While the KBS cathode showed a slopy plateau with immediate decrease in the cell voltage, this step started to proceed at a relative constant voltage in the $KBS_{1-x}Se_x$ cathodes. Especially for the cathodes with high Se content, i.e., $KBS_{0.86}Se_{0.14}$ and $KBS_{0.62}Se_{0.38}$, prominent discharge plateaus were obtained. The enhanced kinetics in case of the Se-doped cathodes led to a higher capacity of 1200 mAh g^{-1} for $KBS_{0.86}Se_{0.14}$ and thereby a higher S utilization. However, as Se has a much larger atomic weight than S, further increase the Se content resulted in a decrease of the capacity.

During the subsequent charging, the continuous conversion from short-chain to long-chain polysulfide/-selenide and finally elemental $S_{1-x}Se_x$ gave rise to a single plateau at ≈1.7 V. As shown in Figure 2a, the KBS cathode suffered from severe overcharging, mainly due to the shuttle effect of soluble polysulfide intermediates.[19] In comparison, voltage rising at the end of charging process got more prominent with the involvement and increase of the Se content, demonstrating less overcharging and thus a higher Coulombic efficiency. Moreover, there was a considerable decrease of voltage hysteresis for the S/Se redox, from 0.82 V in the KBS cathode to 0.70, 0.53, and 0.37 V in the $KBS_{0.92}Se_{0.08}$, $KBS_{0.86}Se_{0.14}$, and $KBS_{0.62}Se_{0.38}$ cathodes, respectively, reflecting an improved reversibility and energy efficiency.

Notably, a simultaneous improvement of the anode process was observed as depicted in Figure 2b. Although the overpotentials for Mg plating/stripping were large with both the KBS and the $KBS_{0.92}Se_{0.08}$ cathode, a significant drop of the value by 0.1 and 0.2 V was measured for the cells with the $KBS_{0.86}Se_{0.14}$ and $KBS_{0.62}Se_{0.38}$ cathode, respectively. To find out the reason, we collected ultraviolet-visible (UV–vis) spectra of the electrolyte cycled with the $KBS_{1-x}Se_x$ cathodes as shown in Figure S5 (Supporting Information). In the first discharged state, major absorbance bands were present in the range of 210–320 nm, corresponding to long-chain polysulfides.[20] Compared to the electrolytes with the KBS and the $KBS_{0.92}Se_{0.08}$ cathode, the absorption peaks are only half in intensity in case of the $KBS_{0.86}Se_{0.14}$ and $KBS_{0.62}Se_{0.38}$ cathode. Based on these results, the reduction of the anode overpotential can be attributed to less dissolution of polysulfide/-selenide into the electrolyte due to the fast conversion of the cathode materials with a higher Se content.

Furthermore, electrochemical tests of the $KBS_{1-x}Se_x$ cathodes were carried out in two-electrode coin cells, applying the same cut-off voltage and charging rate. As shown in Figure 2c, the KBS cathode suffered from the early cell failure at the 10th cycle, which typically occurred during cell charging (see Figure S6, Supporting Information). As revealed in our recent study, such failure is mainly associated with anode processes, where soluble

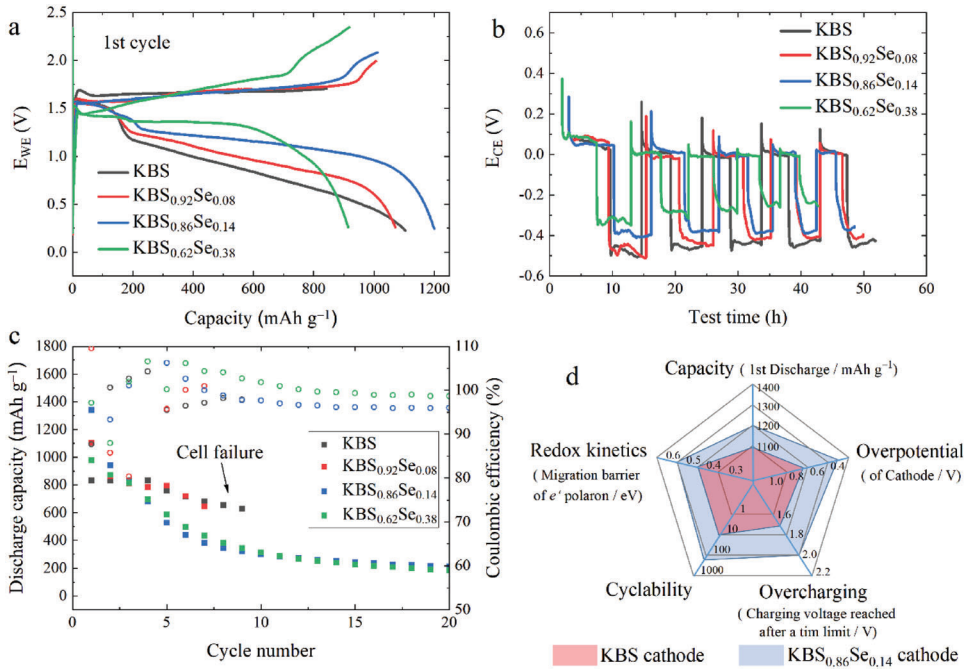

Figure 2. Galvanostatic cycling of the S–Se cathodes and the bare S cathodes in three-electrode Mg cells: a) E_{WE} versus capacity in the first cycle; b) E_{CE} versus time in the first five cycles. The cell was cycled at 0.1 C (168 mA g^{-1}) between 0.2 and 2.7 V versus E_{CE}. c) Cycling performance of KBS and $KBS_{1-x}Se_x$ cathodes in two-electrode coin cells. d) A Radar chat compares the performance metrics between the pure S cathode and the $KBS_{0.86}Se_{0.14}$ cathode. The migration barrier of e' polaron in one of the end products MgS_2 (or $MgSe_2$) was used as an indicator to describe redox kinetics. The data was acquired by DFT calculation as shown in a later section.

polysulfide species induce inhomogeneous Mg deposition and thereby triggering the soft short-circuit.[21] While 8% Se doping to the S cathode did not improve the cyclability, the $KBS_{1-x}Se_x$ cathodes with higher Se contents exhibited a much longer cycle life with a Coulombic efficiency >95%. As shown in Figure S7 (Supporting Information), the $KBS_{0.86}Se_{0.14}$ cathode could be cycled for >200 cycles without short-circuit. Considering the reduced anode overpotential (cf. Figure 2b), the improvement of cyclability might hint at a more homogeneous anode reaction, which will be discussed in a later section. Nevertheless, fast capacity fading was also evident, which needs to be further addressed.

Overall, the kinetics of S redox is significantly enhanced with Se doping, leading to a simultaneous improvement of the achievable capacity and cyclability, but also a reduced voltage hysteresis for charge/discharge and less overcharging. As a result, the $S_{1-x}Se_x$ compounds can be considered as a better benchmark than the bare S cathode toward high-energy Mg–S batteries. Among the tested compositions, the $KBS_{0.86}Se_{0.14}$ cathode offers superior electrochemical performance (see Figure 2d). Considering that Se doping reduces the high theoretical capacity and sustainability of S cathode, the $KBS_{0.86}Se_{0.14}$ cathode with a relatively low Se doping level was chosen as the optimal composition for further investigations.

2.3. Redox Mechanism of the Se–S Cathodes and the Impact on the Mg Anode

Therefore, mechanistic investigation of the redox processes in the Se-S compounds was further conducted with the $KBS_{0.86}Se_{0.14}$ cathodes. **Figure 3** compares the XPS S2p spectra of the $KBS_{0.86}Se_{0.14}$ cathode and the KBS cathode at different states of charge. The pristine $KBS_{0.86}Se_{0.14}$ electrode showed similar spectral profile as the composite (cf. Figure 1), with typical elemental S signals at 163.8 eV and peaks for Se–S interaction at 162.2 eV (see Figure 3b). During the first discharge, all these peaks got vanished, meanwhile new doublets at lower binding energies of 161.9 and 160.9 eV emerged, which correspond to S-S interaction of Mg polysulfide (MgS_n) and Mg–S interaction for MgS, respectively. The disappearance of S^0 signals and the formation of MgS as the major product suggested a high degree of conversion of the active species, reflecting a high utilization of S in the presence of Se and therefore a high capacity was obtained. Whereas for the KBS cathode (Figure 3a), substantial amount of S^0 species remained after fully discharge in the first cycle. Additionally, the conversion was largely limited to the polysulfide intermediates (strong S–S signals) rather than the end product (MgS), indicating only partial reduction of S.

It is worth to note that the reduction of S further proceeded even during the subsequent charging in the KBS cathode, as revealed by the weakening of the S^0 peaks and the strengthening of the Mg–S signals. This explains the overcharging behavior observed in this system (see Figure 2a), where re-oxidation of the active species could hardly take place. Based on the oxidation state of S, the measured charge capacity in the first cycle might be contributed almost entirely by side reactions, rather than the desired S redox reaction. Despite less overcharging in case of the $KBS_{0.86}Se_{0.14}$ cathode, oxidation of S during the first charging process was also hindered as demonstrated in the respective spectra. One possible reason for the low reversibility in the first cycle is

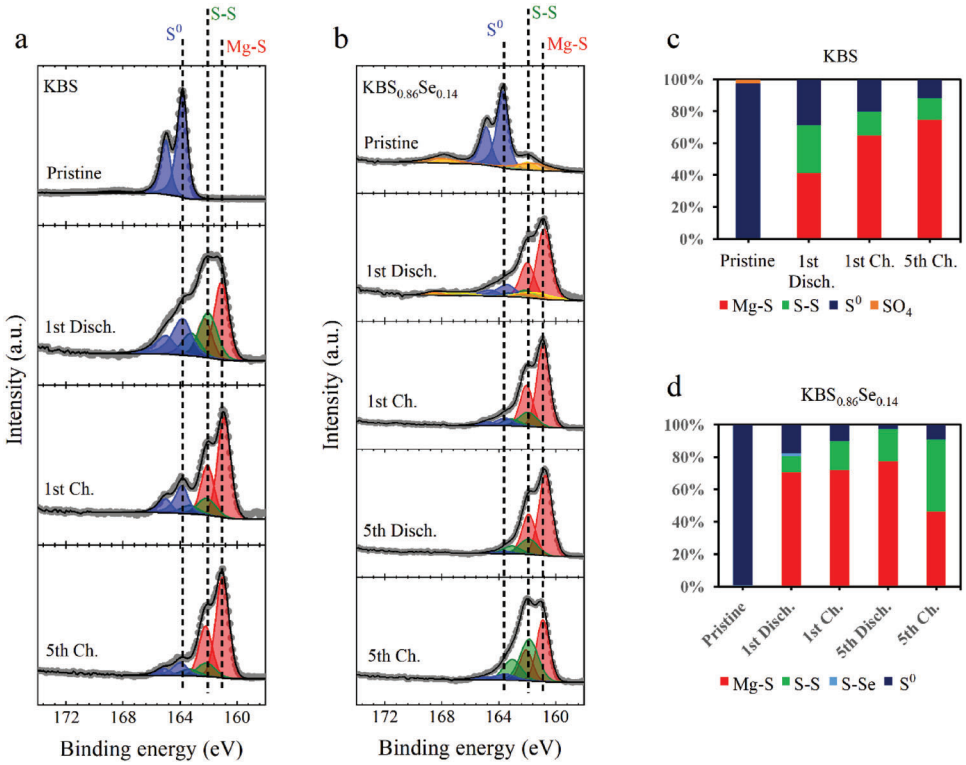

Figure 3. XPS S 2p spectra of the KBS a) and the $KBS_{0.86}Se_{0.14}$ b) cathode at different states of charge. Relative atomic percent of the respective species in the KBS c) and the $KBS_{0.86}Se_{0.14}$ d) cathode, based on XPS data.

the severe side reactions at Mg anode side, due to the shuttling of polysulfide, which is clarified later in this work.

Reversible S conversion was evident in the spectra of the $KBS_{0.86}Se_{0.14}$ cathode in the 5th cycle. While the discharged spectrum showed a high content of MgS, amounting to ≈80% of all the S species, partial oxidation of MgS was observed in the charged spectrum, with the increase of the S–S signals and decrease of the Mg–S signals. As shown in Figure 3d, nearly half of the MgS has been converted back to mainly MgS_n, and partially to S^0. In comparison, Mg–S signals further increased at the 5th charged state, revealing MgS remained as the major species in the KBS cathode (Figure 3c). The difference hints at higher reversibility of the $KBS_{0.86}Se_{0.14}$ cathode in the presence of Mg^{2+}, probably due to faster kinetics of S redox with Se doping and thereby less polysulfide dissolution as indicated by the UV–vis investigation (see Figure S5, Supporting Information).

Nevertheless, as S/Se could hardly convert back to their elemental state, polysulfide/-selenide served as new redox active species for further cycling. This argument was supported by UV–vis study of the electrolyte cycled with the $KBS_{0.86}Se_{0.14}$ cathode at different states of charge. As shown in Figure S8 (Supporting Information), the absorption peaks for polysulfide species evolved when cycling the cell: In the 5th cycle, the intensity of the respective peaks increased significantly upon charging, indicating the formation of long-chain polysulfide. On the other hand, the development of polysulfide content in the electrolyte also reflected the changes in cathode capacity. A constant decrease of the peaks for polysulfide in the UV–vis spectra over cycling (compare the 5th Ch. and the 20th Ch.) suggested a continuous loss of active species, which is the main reason for the capacity fading.

In fact, the loss of Se was evident in the XPS Se 3d spectra of the $KBS_{0.86}Se_{0.14}$ cathode at selected states of charge (Figure S9, Supporting Information), where a sharp decrease of the Se signals (both Se-S and Se-Se interactions) was observed only after the initial discharge. In the further cycling process, the Se signals could not be detected from the cathode anymore, but was found at Mg anode after 20 cycles by EDX (Figure S10, Supporting Information), with a similar content as S. The shuttling of polyselenide in the Se-dope S cathodes could be mitigated by a proper design of the carbon matrix, due to the different binding strength of polyselenide and polysulfide.[22] Alternatively, further development of electrolytes that suppress polysulfide dissolution, or even lead to solid conversion of the S-Se compounds would ultimately solve this issue.[23] Although beyond the scope of this study, these strategies deserve further efforts in improving the performance of the system, toward practical high-energy Mg–S batteries.

Due to the polysulfide-/selenide shuttling, we further examined their crossover effect on the Mg anode. In order to gain insights into the degradation mechanism, we investigated the Mg anodes after cycling in the Mg–S cells with either the KBS cathode or the $KBS_{0.86}Se_{0.14}$ cathode, by means of time-of-flight secondary ion mass spectrometry (ToF-SIMS). As evidenced by static ToF-SIMS in **Figure 4a**, surfaces of both electrodes showed strong sulfur signals in negative secondary ion (SI) polarity. In addition, Se signals were also present in the Mg anode cycled with the

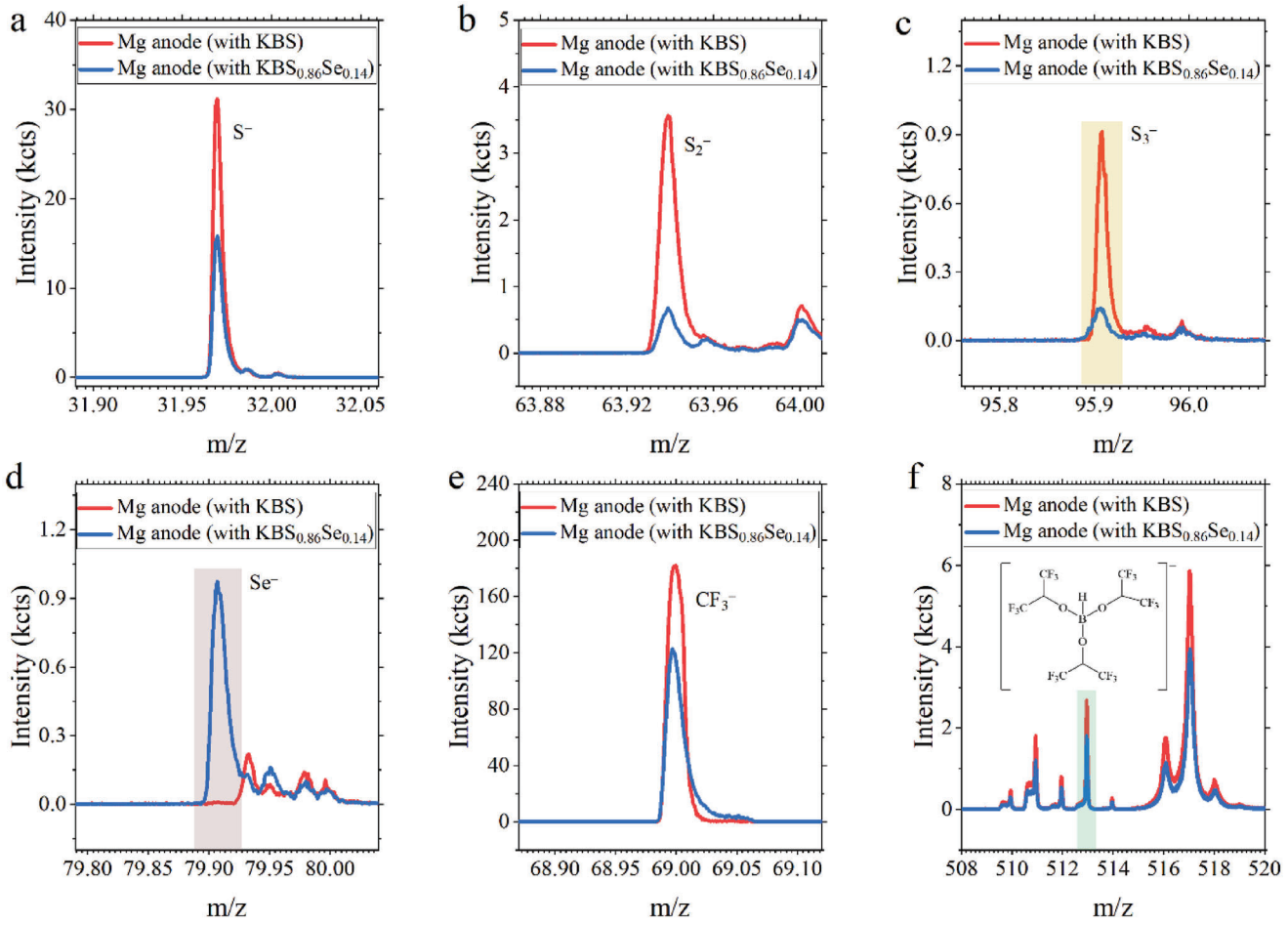

Figure 4. Static ToF-SIMS analysis of the Mg anode after five cycles against the KBS (red) and the $KBS_{0.86}Se_{0.14}$ cathode (blue). All raw data can be found at DOI: 10.35097/924.

Se-doped cathode (Figure 4d), as demonstrated by the characteristic isotope pattern in Figure S11 (Supporting Information).

The presence of redox active cathode components at Mg surface confirmed the shuttling of S and Se species. Besides showing a stronger S^- signal, peaks related to S_2^- and S_3^- were also detected to be stronger on the Mg anode cycled with the KBS cathode (Figure 4b,c), indicating more polysulfide at the top surface. Considering the probing depth of the static SIMS (first 5 nm), the stronger signals could result from a higher concentration of the polysulfide in the electrolyte in case of the KBS cathode. This speculation is further supported by the presence of intact electrolyte species $BO_3C_9H_4F_{18}^-$ found at 513 m/z (Figure 4f) and its fragment CF_3^- at 69 m/z (Figure 4e). In positive SI polarity (Figure S12, Supporting Information), MgF^+, BO_2^+ and other B species from the electrolyte were detectable, also confirming the electrolyte residue on the anode surface.

Moreover, substantial amount of corrosion pits were found on the cycled Mg anodes, which were presumably formed by Mg plating/stripping.[24] In **Figure 5**a, scanning electron microscope (SEM) image of the sample cycled against the KBS cathode showed large corrosion cavities (dark area) resulted from agglomeration of small pits, indicating continuous anode reaction limited to certain areas of the anode surface. In comparison, smaller corrosion spots were distributed uniformly on the Mg anode coupled with the $KBS_{0.86}Se_{0.14}$ cathode (see Figure 5b), leading to a more homogeneous and denser deposition. The larger redox active surface and more uniform deposition morphology ensure smoother anode reactions, which explains longer cyclability of the $KBS_{0.86}Se_{0.14}$–based cell than the KBS–based cell.

Further, surface of the cycled Mg anodes in spots and spot-poor areas were separately analyzed. To minimize the influence of electrolyte residue, dynamic ToF-SIMS (dual beam depth profiling) was performed. Figure 5c,d show the depth integrated images of representative species in the spotted area of the Mg anodes, while their full portfolios of measured species are present in Figures S14 and S16 (Supporting Information), respectively. The isotope $^{34}S^-$ signals were used to demonstrate the distribution of S species, due to detector saturation for the more abundant main isotope $^{32}S^-$ signals. On both Mg anodes, strong S signals were found mostly in the dark spots, where anode reactions were taking place. As fresh Mg with high reactivity was formed during plating/stripping, Mg polysulfide tended to be accumulated and immobilized in these area. A similar distribution was observed for Se species in case of the Se-doped sample. As demonstrated in the scatter plot in Figure 5f, there is a strong correlation between S and Se species. In addition to S and Se signals, other

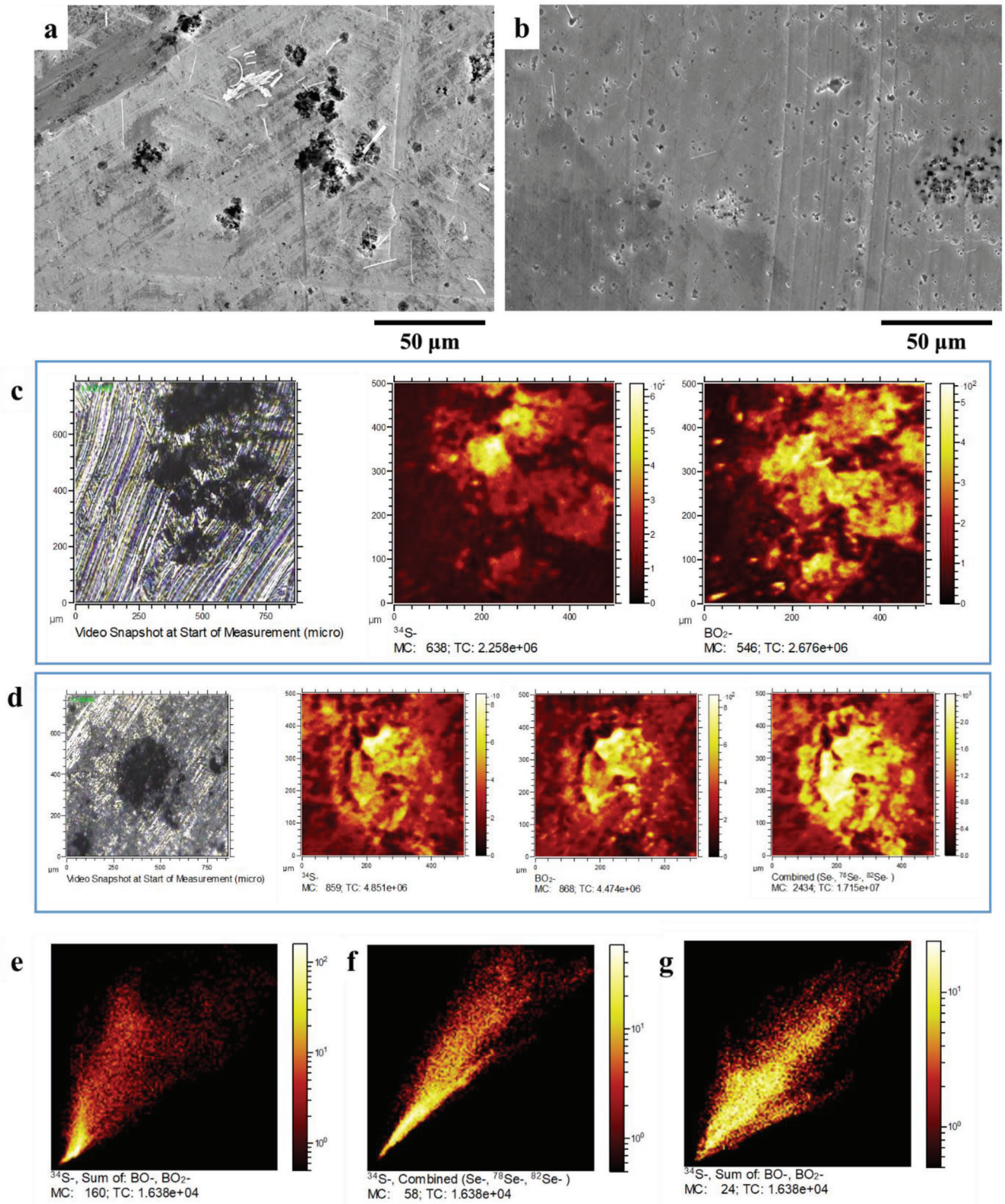

Figure 5. Typical SEM images of the Mg anodes after 5 cycles against the a) KBS and b) the $KBS_{0.86}Se_{0.14}$ cathode. ToF-SIMS depth integrated images of the Mg anodes with c) the KBS and d) the $KBS_{0.86}Se_{0.14}$ cathode in the spotted area. Scatter plot of the Mg anode with the KBS cathode: correlation between e) $^{34}S^-$ and BO_x^- signals. Scatter plot of the Mg anode with the $KBS_{0.86}Se_{0.14}$ cathode: correlation between f) $^{34}S^-$ and Se^- signals, g) and $^{34}S^-$ and BO_x^- signals.

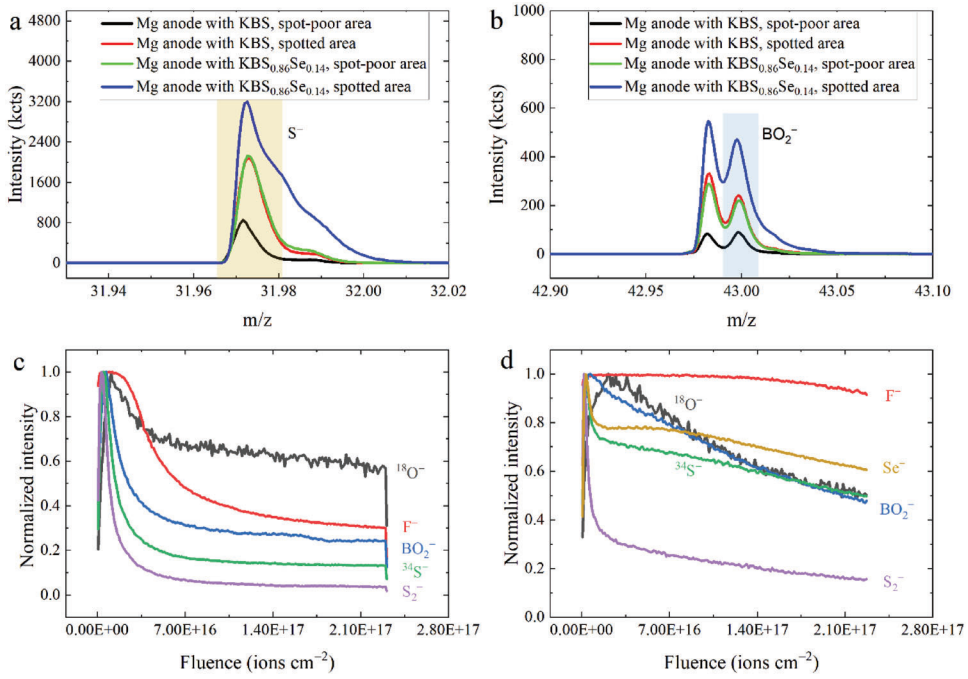

Figure 6. ToF-SIMS depth integrated spectra of the Mg anodes in spotted area and spot-poor area: a) S^- signals and b) BO_2^- signals. Depth profiles of the Mg anodes with c) KBS and d) $KBS_{0.86}Se_{0.14}$ cathode in spotted areas.

species such as $^{18}O^-$, BO_x^- and F^- were also concentrated in the spotted area, which were originated from the electrolyte.

In the Mg anode with the $KBS_{0.86}Se_{0.14}$ cathode, correlation between the S/Se species and the electrolyte fragments in spatial distribution was found in Figure 5g, indicating side reactions involving simultaneous electrolyte decomposition and S immobilization. However, such correlation was weak in the Mg anode with the KBS cathode (Figure 5e), probably due to the complicated morphological structure of the spotted area, resulting in the presence of a mixture of pristine electrolyte and its decomposition products. Whereas for the spot-poor areas, all the measured fragments exhibited relative uniform distribution in the selected region (Figures S13 and S15, Supporting Information).

Figure 6a compares the depth integrated spectra of the Mg anodes with the KBS and the $KBS_{0.86}Se_{0.14}$ cathode in spotted area and spot-poor area. Eroded with identical Cs dose densities, the Mg anode cycled with the $KBS_{0.86}Se_{0.14}$ cathode has the highest sulfur signal in the spotted area. Even the spot-poor area in the same sample showed a comparable intensity of S signals to the sample cycled with the KBS cathode at the spotted area. The result seemed to be contradict with the static ToF-SIMS data, where the Mg anode with the $KBS_{0.86}Se_{0.14}$ cathode showed a lower S signals. In fact, as ToF-SIMS is surface sensitive (measured depth ≈5 nm), the static data indicated a sulfur-poor layer at top-most surface of the Mg anode, reflecting a lower polysulfide concentration in the electrolyte. Accordingly, the amount of MgS_x precipitated on Mg within each cycle was smaller, which allowed further Mg plating/stripping in the same region. As evident in Figure 6d, the S^- signals was still relatively high after 30 min erosion toward the bulk of Mg anode. Therefore, the cumulative signals presented in Figure 6a was high. Whereas in the cell with KBS cathode, a sulfur-rich layer was formed on the very surface of Mg, which impeded further anode reactions. As a result, the reaction depth at Mg anode was limited (Figure 6c) and the plating/stripping of Mg was inhomogeneous (Figure 5a). Besides polysulfide shuttling, electrolyte decomposition was also found more prominent in the Se-doped sample, as evidenced by stronger signals of typical electrolyte fragment BO_2^- (see Figure 6b). In the depth profiles in Figure 6d, signals of both BO_2^- and F^- species were still present even after applying a high sputter ion fluence. Overall, the ToF-SIMS study revealed S immobilization and electrolyte decomposition at Mg anode as the main reason for the capacity fading.

2.4. Electronic and Ionic Transport in Redox End-Products

While the experimental mechanistic study confirmed the improved kinetics of S conversion, we further used density functional theory (DFT) calculations to analyze the charge transport in the redox end-products in the Se-doped S cathode and how that can explain the improved performance of the system. As a first step, we developed cluster expansion models coupled with DFT calculations to determine whether the Se doping in S results in redox end-products as a solid solution or separate phases for magnesium chalcogenides (i.e., solid solution as $MgS_{1-x}Se_x$ or two-phase as MgS/MgSe) and magnesium dichalcogenides (i.e., solid solution as $MgS_{2-x}Se_x$ or two-phase as $MgS_2/MgSe_2$). We constructed separate cluster expansion models for magnesium chalcogenides (rocksalt and zinc blend),[4d] and magnesium dichalcogenides (cubic pyrite) by varying the S and Se concentration. The convex hull plot (Figure S18, Supporting Information) from the cluster expansion calculations suggest that the redox end-products prefer to be in different phases such as rocksalt

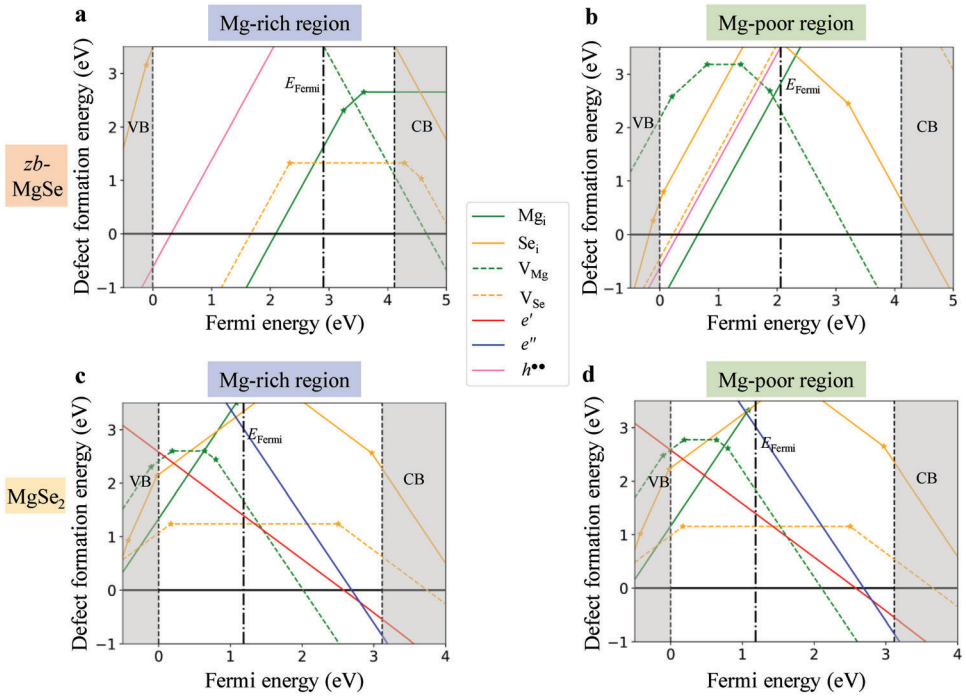

Figure 7. Defect formation energy diagram for various intrinsic defects in MgSe and $MgSe_2$. The left panel (a,c) illustrate the formation energy in Mg-rich condition, and the right panel (b,d) shows the formation energy in Mg-poor condition.

MgS (*rs*-MgS), zinc blend MgSe (*zb*-MgSe), MgS_2, and $MgSe_2$ rather than forming solid solution. However, it is worth noting that the formation energy for structures at intermediate concentration are quite low and near to the convex hull. This is particularly relevant in the case of magnesium dichalcogenides. It is very likely that $(S–Se)^{2-}$ dimers are present in MgS_2 as impurities, replacing S^{2-} dimers. The explanation for this is the following: The Se in Se-doped sulfur forms part of S_7Se rings. When the S_7Se rings start to break into smaller polysulfide during the battery operation, eventually $(S\text{-}Se)^{2-}$ dimers will be formed. To form phase separated magnesium dichalcogenides the $(S\text{-}Se)^{2-}$ dimers should break and then recombine with other broken $(S\text{-}Se)^{2-}$ dimers to form S_2^{2-} and Se_2^{2-} dimers. Such a process is foreseen to have large kinetic barriers, and thus it is more likely that $(S\text{-}Se)^{2-}$ dimers enter as impurities in MgS_2.

The next step is to identify the charge transport in the redox end-products. The charge transport mechanism in *rs*-MgS and MgS_2 has already been studied.[25] Thus, our focus is to study the charge transport in *zb*-MgSe and $MgSe_2$. We study the contributions of several intrinsic defects to the conductivity of *zb*-MgSe and $MgSe_2$. Several charged defects including Mg interstitial (Mg_i), Se interstitial (Se_i), Mg vacancy (V_{Mg}), Se Vacancy (V_{Se}), and polarons are considered. In the case of *zb*-MgSe, only hole polarons were able to localize, and in the case of $MgSe_2$ we were able to localize single electron (e') polaron and double electron (e'') polaron.

Kroger–Vink notation is used to denote the defect type and associated charges. The charges associated with the defects are given in the superscript of the notation (• for a positive charge, ′ for a negative charge, and x for a neutral fault). The defect formation energies are computed for Mg-rich region (left panel in **Figure 7**) and Mg-poor region (right panel in Figure 7). The slope of the line defines the charge of the respective defect. A positive slope represents the formation energy of the positive charged defect, while a negative slope represents the formation energy of negative charged defect. A neutral defect has a zero slope. The vertical dashed-dotted line represents the equilibrium fermi level (E_{Fermi}). The defects with low energy of formation at E_{Fermi} are considered as thermodynamically most preferred defects. The formation energy and concentration of the most favorable defects in *zb*-MgSe and $MgSe_2$ is given in **Table 1**.

V_{Se}^{x} is the most prevalent defect in *zb*-MgSe at Mg-rich region; however, since it is a neutral defect, it does not contribute to charge transport and is therefore disregarded in further analysis. The most favourable charge defect at Mg-rich region is $Mg_i^{\bullet\bullet}$ with a defect concentration of 4×10^{-5} cm^{-3}. Whereas, the most prevalent charge defect at Mg-poor region is V_{Mg}'', which having a relatively large defect formation energy that leads to a very low concentration of 3×10^{-17} cm^{-3}. In the case of $MgSe_2$, V_{Se}^{x} is the prevalent defect in both Mg-rich and Mg-poor regions, which do not contribute to the charge transport. The e' polaron and V_{Mg}'' are the prevalent charge defects in $MgSe_2$ with defect concentrations of 1×10^{-1} and 4×10^{-6} cm^{-3}, respectively.

The next step is to analyze the mobility and conductivity associated with the prevalent charge defects in *zb*-MgSe and $MgSe_2$. Table 1 shows the calculated migration barrier, mobility, conductivity associated with the prevalent charge defects. All of the prevalent charge defects exhibit high migration barrier, resulting in very limited mobility. In *zb*-MgSe, V_{Mg}'' has relatively lower migration barrier, however due to their low concentration, they results in very low conductivity. On the other hand, the e' polaron

Table 1. Calculated formation energies, defect concentrations, energy barriers, mobilities, and conductivities at 300 K for the prevalent defects in MgSe and $MgSe_2$.

System	Defect	Formation energy [eV]	Concentration [cm^{-3}]	Migration barrier [eV]	Mobility [$cm^2\ V^{-1}s^{-1}$]	Conductivity [$S\ cm^{-1}$]
zb-MgSe	V''_{Mg}	2.31	3×10^{-17}	0.86	5×10^{-15}	4×10^{-50}
	$Mg_i^{\bullet\bullet}$	1.63	4×10^{-5}	1.07	1×10^{-18}	2×10^{-41}
$MgSe_2$	V''_{Mg}	1.64	4×10^{-6}	2.04	7×10^{-35}	9×10^{-59}
	e'	1.39	1×10^{-1}	0.74	3×10^{-13}	5×10^{-33}

in $MgSe_2$ exhibits relatively low migration barrier and results in a high mobility of 3×10^{-13} $cm^2\ V^{-1}\ s^{-1}$.

The large migration barrier associated with these prevalent defects makes it difficult for the charge defects to diffuse through the system. That means the contribution of these prevalent defects to the charge transport in *zb*-MgSe and $MgSe_2$ is negligible. Previous work on charge transport in $MgSe_2$, demonstrated that charge transport can happen in the material via an e' polaron diffusion with a migration barrier of 0.53 eV.[25] Despite the fact that our cluster expansion calculation indicates that the system tends to be in distinct phases than the solid solution, the formation energy for the intermediate concentrations is extremely low.

Having shown that the charge transport in *zb*-MgSe and $MgSe_2$ is negligible, and thus the formation of such products cannot be the explanation for the improved performance of the system, we turn back to the impact of the presence of $(S\text{-}Se)^{2-}$ dimer impurities in MgS_2 discussed above. Consequently, we also investigated the diffusion of e' polaron in a $(S\text{-}Se)^{2-}$ dimer doped MgS_2 system. The diffusion of e' polaron localized on S-Se to S-S was investigated. The minimum energy path for the diffusion of e' polaron is depicted in **Figure 8**. The diffusion of e' polaron exhibits a low migration barrier of 0.45 eV (i.e., 0.08 eV lower than for pure MgS_2), indicating that the $(S\text{-}Se)^{2-}$ dimer impurities may enhance the charge transport in MgS_2. The low migration barrier facilitates the diffusion of charge, which enhances the performance of the battery as observed in the experiment.

2.5. Strategies to Improve the Capacity Retention

$$MgS_n + Mg\,(0) \rightarrow MgS_{n-2} \quad (\text{self} - \text{discharge, chemical reaction}) \quad (1)$$

$$MgS_n + 2\,e^- \rightarrow MgS_{n-2} \quad (\text{electrochemical reduction}) \quad (2)$$

Although the $KBS_{0.86}Se_{0.14}$ cathode showed improved cyclability, the capacity fading was still severe. As revealed by the mechanistic investigations, polysulfide/-selenide shuttling to the Mg anode results in a loss of active material, which could be the main reason for capacity fading. The S species can be accumulated on the anode either by self-discharge or through electrochemical reduction during cell charging (see Equation (1) and (2)). The self-discharge in Mg–S batteries is a fast chemical process,[26] which is independent of the status of the cell (in static or dynamic condition). Therefore, the $KBS_{0.86}Se_{0.14}$ cathode was also tested at a higher C-rate of 0.5C, hoping to minimize the chemical reaction at anode by faster S conversion. In **Figure** 9a, the charge-discharge profile of 0.5C showed less pronounced but still distinct plateaus in the first cycle, with slightly increased

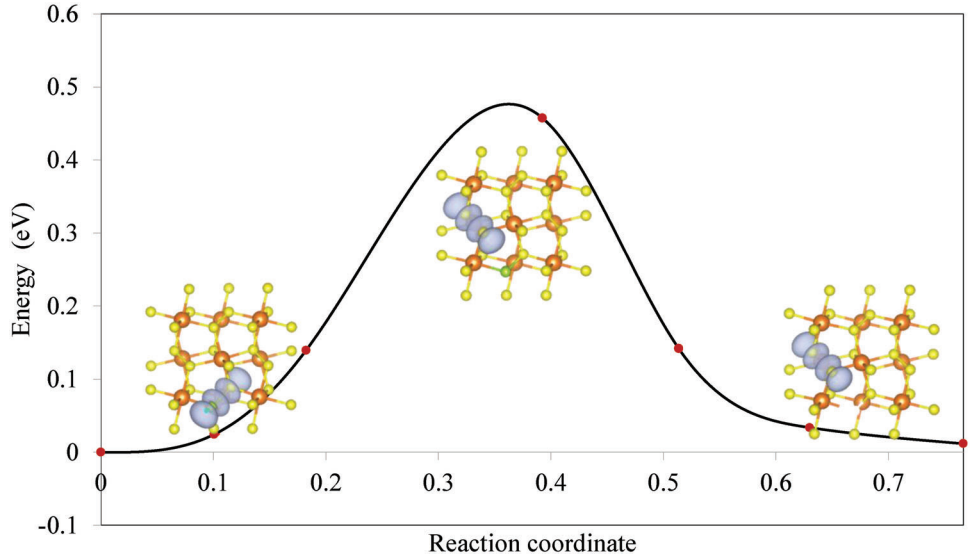

Figure 8. Minimum energy path for the diffusion of e' polaron diffusion in Se-doped $MgSe_2$. The magnetization density at initial, intermediate and final states are also shown in the figure. The Mg, S, and Se atoms are show in brown, yellow, and green color, respectively.

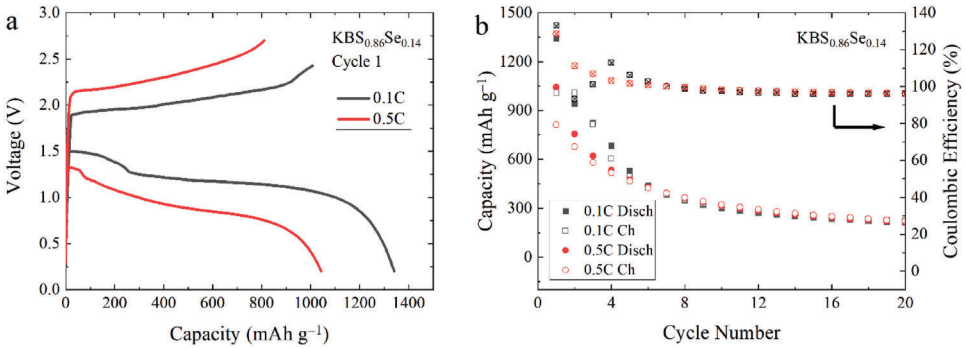

Figure 9. Cycling of $KBS_{0.86}Se_{0.14}$ cathode at different C-rates: a) voltage profile; b) cycling performance.

overpotential compared to the cell charging at 0.1C. The cathode delivered an initial capacity exceeding 1000 mAh g^{-1}, close to 80% of the capacity of 0.1C, demonstrating a good rate capability. However, there was a similar rate of capacity fading irrespective of the C-rate, as evident in Figure 9b. The result suggests that electrochemical reduction of S at anode to be mainly responsible for the capacity fading over cycling. Furthermore, additional galvanostatic test of the $KBS_{0.86}Se_{0.14}$ cathode was carried out, with no time limit for charging. As shown in Figure S17 (Supporting Information), the discharge capacity dropped to ≈230 mAh g^{-1} after 20 cycles, which was similar to the cells tested with a time limit (Figure 9b).

To avoid the parasitic anode reactions, strategies that prevent Mg polysulfide to migrate from the cathode side to the anode can be an effective solution. In this regard, separator coating has proven to be a viable approach.[27] As reported by Xue et al., Mo_6S_8 exhibited a high affinity to lithium polysulfide.[28] We transferred the concept to Mg chemistries,[19] and developed a functional separator with a thin coating of Chevrel phase Mo_6S_8. The investigation revealed a strong adsorption ability of Mo_6S_8 for Mg polysulfide with a binding energy more than 2 eV (the value for carbon could hardly reach 1 eV). In addition, Mo_6S_8 showed a catalytic effect with a reduced energy barrier for polysulfide conversion. Therefore, the Mo_6S_8 modified separator could be beneficial for the capture and conversion of Mg polysulfide, and was further implemented in the cell with the $KBS_{0.86}Se_{0.14}$ cathode. As shown in **Figure 10**a, the $KBS_{0.86}Se_{0.14}$ cathode with modified separator exhibited a typical two-plateau feature of the S/Se redox, delivering a capacity of 1400 mAh g^{-1} in the first cycle, which is similar to the cathode with the bare separator. Improvement of the capacity retention was evident by comparing the voltage profiles in the subsequent cycles. While the $KBS_{0.86}Se_{0.14}$ cathode with modified separator showed relative stable capacity of 900 mAh g^{-1} in the 3rd and 5th cycle, the cathode with the bare separator exhibited a sharp drop of capacity to 800 and 500 mAh g^{-1}, respectively. Figure 10b shows the cycling performance of both the cell configurations, where the use of modified separator could increase the capacity retention significantly from 97 to 158 mAh g^{-1} (>50% increase) at the 200th cycle. After that, the capacity retention became stable, and after 300 cycles a capacity of 149 mAh g^{-1} was retained. Compared to other cathodes for Mg–S batteries (Table S1, Supporting Information), the cycling performance of the $KBS_{0.86}Se_{0.14}$ cathode is found to be encouraging. Particularly the beneficial effects of Se on both electrodes, i.e., increased S utilization at the cathode side (higher initial capacity) and enhanced stability of Mg plating/stripping at the anode side (longer battery life), calls for further optimization of the system. Performance improvement strategies developed in other metal-sulfur systems could be in principle feasible for Mg–S chemistries with the S–Se compounds. As already demonstrated in Mg–S batteries, anode protection[29] or using alternative anode[30] can be effective to increase the capacity retention, and therefore deserves investigation.

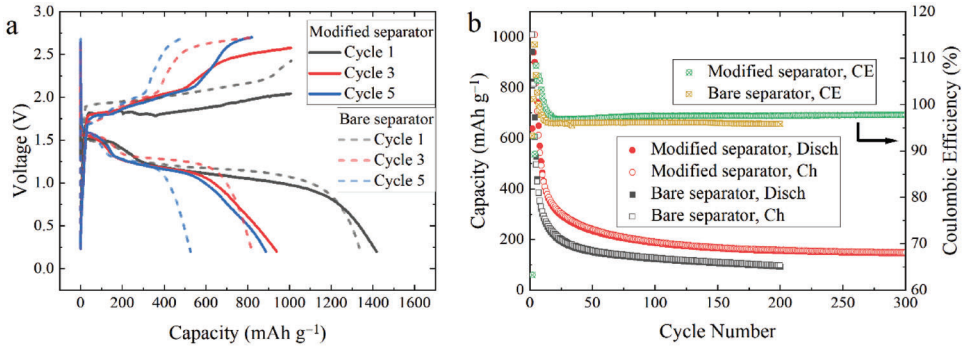

Figure 10. Galvanostatic cycling of $KBS_{0.86}Se_{0.14}$ cathode at 0.1C with (or without) modified separator: a) voltage profiles in the initial cycles; b) cycling performance.

3. Conclusion

In summary, we have demonstrated a doping strategy that, introduces Se to bare S cathode, effectively enhances the redox kinetics of S in Mg–S batteries. Due to their high miscibility, combining insulating elemental S with electrically conductive Se can improve the bulk conductivity of the S cathode by forming a homogeneous solid-solution at molecular level. A systematic investigation of a model KBS cathode and the doped $KBS_{1-x}Se_x$ cathodes via electrochemical tests and spectroscopic analysis reveals the fast conversion of S in the presence of Se, which gives rise to a higher S utilization and less polysulfide dissolution. In addition, computational analysis of the charge transport in redox end-products suggests that Se-doped MgS_2 can maintain electronic conduction through the migration of electron polaron. As a result, the $KBS_{1-x}Se_x$ cathodes provide a largely improved performance metrics, including higher achievable capacity and specific energy, longer cyclability, smaller overpotentials and less severe overcharging. The extended cyclability was attributed to smoother anode reactions, due to a lower content of polysulfide in the electrolyte. Based on the cell performance, an optimized composition $S_{0.86}Se_{0.14}$ was determined, which exhibits the potential to be a better benchmark compound than bare S for Mg–S batteries.

Despite less polysulfide dissolution, the $KBS_{0.86}Se_{0.14}$ cathode still suffers from fast capacity fading. ToF-SIMS study indicates severe side reactions between soluble polysulfide and the Mg anode, with the formation of an interphase layer that immobilizes S at the anode side. To alleviate polysulfide shuttling, a modified separator with Mo_6S_8 coating was applied in the Mg–S cells, which improves the capacity retention by >50% in the longer cycling. At the 300th cycle, the $KBS_{0.86}Se_{0.14}$ cathode delivers a capacity of 149 mAh g^{-1}. The results suggest other improvement strategies that either lead to less polysulfide shuttling or protection of Mg anode could be effective for increasing the capacity retention of the $KBS_{0.86}Se_{0.14}$ cathode. Further development of such strategies might pave the way toward high-energy Mg–S batteries with the S-Se compounds.

Supporting Information

Supporting Information is available from the Wiley Online Library or from the author.

Acknowledgements

The authors acknowledge the funding from Bundesministerium für Bildung und Forschung (BMBF) of Germany via the "MagSiMal" project (03XP0208), and from the European Union's Horizon 2020 research and innovation programme under grant agreement No 824066 via the "E-MAGIC" project. This work contributes to the research performed at CELEST (Center for Electrochemical Energy Storage Ulm-Karlsruhe) and was partly funded by the German Research Foundation (DFG) under Project ID 390874152 (POLiS Cluster of Excellence). This work was partly carried out with the support of the Karlsruhe Nano Micro Facility (KNMFi), a Helmholtz Research Infrastructure at Karlsruhe Institute of Technology (KIT). Z.L. acknowledges the funding by the National Natural Science Foundation of China with grant No 52002350.

Open access funding enabled and organized by Projekt DEAL.

Conflict of Interest

The authors declare no conflict of interest.

Data Availability Statement

SIMS data is available at the Radar4KIT repository, DOI: 10.35097/924, under CC-BY 4.0 license. All experimental data that support the findings of this study are readily available upon reasonable request from the corresponding authors.

Keywords

magnesium–sulfur batteries, selenium doping, sulfur cathodes, sulfur redox, sulfur–selenium compounds

Received: August 31, 2023
Revised: September 12, 2023
Published online:

[1] C.-X.i Zu, H. Li, *Energy Environ. Sci.* **2011**, *4*, 2614.
[2] a) G. Bieker, V. Küpers, M. Kolek, M. Winter, *Commun. Mater.* **2021**, *2*, 37; b) P. He, J. L. Schaefer, *ACS Energy Lett.* **2022**, *7*, 4352.
[3] L. Kong, C. Yan, J.-Q.i Huang, M.-Q. Zhao, M.-M. Titirici, R. Xiang, Q. Zhang, *Energy Environ. Mater.* **2018**, *1*, 100.
[4] a) P. Wang, M. R. Buchmeiser, *Adv. Funct. Mater.* **2019**, *29*, 1905248; b) T. Gao, S. Hou, F. Wang, Z. Ma, X. Li, K. Xu, C. Wang, *Angew. Chem.-Int. Ed.* **2017**, *56*, 13526; c) Z. Zhao-Karger, R. Liu, W. Dai, Z. Li, T. Diemant, B. P. Vinayan, C. Bonatto Minella, X. Yu, A. Manthiram, R. J. Behm, M. Ruben, M. Fichtner, *ACS Energy Lett.* **2018**, *3*, 8; d) B. P. Vinayan, H. Euchner, Z. Zhao-Karger, M. A. Cambaz, Z. Li, T. Diemant, R. J. Behm, A. Gross, M. Fichtner, *J. Mater. Chem. A* **2019**, *7*, 25490.
[5] D.-M. Kim, S. C. Jung, S. Ha, Y. Kim, Y. Park, J.i H. Ryu, Y.-K. Han, K. T. Lee, *Chem. Mater.* **2018**, *30*, 3199.
[6] P. Bonnick, J. Muldoon, *Adv. Funct. Mater.* **2020**, *30*, 1910510.
[7] P. He, H. O. Ford, L. C. Merrill, J. L. Schaefer, *ACS Appl. Energy Mater.* **2019**, *2*, 6800.
[8] L. Zeng, N. Wang, J. Yang, J. Wang, Y. Nuli, *J. Electrochem. Soc.* **2017**, *164*, A2504.
[9] A. Du, Z. Zhang, H. Qu, Z. Cui, L. Qiao, L. Wang, J. Chai, T. Lu, S. Dong, T. Dong, H. Xu, X. Zhou, G. Cui, *Energy Environ. Sci.* **2017**, *10*, 2616.
[10] Q. Zou, Y. Sun, Z. Liang, W. Wang, Y.i-C. Lu, *Adv. Energy Mater.* **2021**, *11*, 2101552.
[11] X. Li, J. Liang, K. Zhang, Z. Hou, W. Zhang, Y. Zhu, Y. Qian, *Energy Environ. Sci.* **2015**, *8*, 3181.
[12] C.-P. Yang, S. Xin, Y.-X. Yin, H. Ye, J. Zhang, Y.-G. Guo, *Angew. Chem.-Int. Ed.* **2013**, *52*, 8363.
[13] R. Cooper, J. V. Culka, *J. Inorg. Nucl. Chem.* **1967**, *29*, 1217.
[14] A. Abouimrane, D. Dambournet, K. W. Chapman, P. J. Chupas, W. Weng, K. Amine, *J. Am. Chem. Soc.* **2012**, *134*, 4505.
[15] a) Z. Zhao-Karger, X.-M. Lin, C. Bonatto Minella, D. Wang, T. Diemant, R. J. Behm, M. Fichtner, *J. Power Sources* **2016**, *323*, 213; b) D.i Wu, W. Ren, Y. Yang, J. Wang, Y. Nuli, *J. Phys. Chem. C* **2021**, *125*, 25959.
[16] Y. Wei, Y. Tao, Z. Kong, L. Liu, J. Wang, W. Qiao, L. Ling, D. Long, *Energy Storage Mater.* **2016**, *5*, 171.
[17] Z. Zhao-Karger, M. E. Gil Bardaji, O. Fuhr, M. Fichtner, *J. Mater. Chem. A* **2017**, *5*, 10815.

[18] a) R. Fang, S. Zhao, Z. Sun, D.-W. Wang, H.-M. Cheng, F. Li, *Adv. Mater.* **2017**, *29*, 1606823; b) S. S. Zhang, *J. Power Sources* **2013**, *231*, 153.
[19] L. Wang, P. Jankowski, C. Njel, W. Bauer, Z. Li, Z. Meng, B. Dasari, T. Vegge, J. M. G. Lastra, Z. Zhao-Karger, M. Fichtner, *Adv. Sci.* **2022**, *9*, 2104605.
[20] a) G. Bieker, D. Diddens, M. Kolek, O. Borodin, M. Winter, P. Bieker, K. Jalkanen, *J. Phy. Chem. C* **2018**, *122*, 21770; b) J. Häcker, D. H. Nguyen, T. Rommel, Z. Zhao-Karger, N. Wagner, K. A. Friedrich, *ACS Energy Lett.* **2022**, *7*, 1.
[21] L. Wang, T. Diemant, Z. Li, B. Dasari, Z. Zhao-Karger, *ACS Appl. Energy Mater.* **2023**, *6*, 1008.
[22] G.-L. Xu, T. Ma, C.-J. Sun, C. Luo, L. Cheng, Y. Ren, S. M. Heald, C. Wang, L. Curtiss, J. Wen, D. J. Miller, T. Li, X. Zuo, V. Petkov, Z. Chen, K. Amine, *Nano Lett.* **2016**, *16*, 2663.
[23] G.-L. Xu, H. Sun, C. Luo, L. Estevez, M. Zhuang, H. Gao, R. Amine, H. Wang, X. Zhang, C.-J. Sun, Y. Liu, Y. Ren, S. M. Heald, C. Wang, Z. Chen, K. Amine, *Adv. Energy Mater.* **2019**, *9*, 1802235.
[24] X. Liu, A. Du, Z. Guo, C. Wang, X. Zhou, J. Zhao, F.u Sun, S. Dong, G. Cui, *Adv. Mater.* **2022**, *34*, 2201886.
[25] S. Vincent, J. H. Chang, P. Canepa, J. M. García-Lastra, *Chem. Mat.* **2023**, *35*, 3503.
[26] D. Bosubabu, Z. Li, Z. Meng, L.-P. Wang, M. Fichtner, Z. Zhao-Karger, *J. Mater. Chem. A* **2021**, *9*, 25150.
[27] a) Y. Yang, W. Fu, D. Zhang, W. Ren, S. Zhang, Y. Yan, Y. Zhang, S.-J. Lee, J.-S. Lee, Z.-F. Ma, J. Yang, J. Wang, Y. Nuli, *ACS Nano* **2023**, *17*, 1255; b) Y. Ji, X. Liu-Théato, Y. Xiu, S. Indris, C. Njel, J. Maibach, H. Ehrenberg, M. Fichtner, Z. Zhao-Karger, *Adv. Funct. Mater.* **2021**, *31*, 2100868.
[28] W. Xue, Z. Shi, L. Suo, C. Wang, Z. Wang, H. Wang, K. P. So, A. Maurano, D. Yu, Y. Chen, L. Qie, Z. Zhu, G. Xu, J. Kong, J. Li, *Nat. Energy* **2019**, *4*, 374.
[29] J. Häcker, T. Rommel, P. Lange, Z. Zhao-Karger, T. Morawietz, I. Biswas, N. Wagner, M. Nojabaee, K. A. Friedrich, *ACS Appl. Mater. Interfaces* **2023**, *15*, 33013.
[30] Z. Meng, D. Foix, N. Brun, R. Dedryvère, L. Stievano, M. Morcrette, R. Berthelot, *ACS Energy Lett.* **2019**, *4*, 2040.